

AGN - host galaxy photometric decomposition using a fast, accurate and precise deep learning approach

B. Margalef-Bentabol¹*, L. Wang^{1,2}, A. La Marca^{1,2}, and V. Rodriguez-Gomez³

¹ SRON Netherlands Institute for Space Research, Landleven 12, 9747 AD Groningen, The Netherlands

² Kapteyn Astronomical Institute, University of Groningen, Postbus 800, 9700 AV Groningen, The Netherlands

³ Instituto de Radioastronomía y Astrofísica, Universidad Nacional Autónoma de México, Apdo. Postal 72-3, 58089 Morelia, Mexico

Received -; accepted -

ABSTRACT

Aims. Identification of active galactic nuclei (AGNs) is extremely important for understanding galaxy evolution and its connection with the formation and evolution of supermassive black holes (SMBH). With the advent of deep and high angular resolution imaging surveys such as those conducted with the *James Webb* Space Telescope (JWST), it is now possible to identify galaxies with a central point source out to the very early Universe. In this proof of concept study, we aim to develop a fast, accurate and precise method to identify galaxies which host AGNs and recover the intrinsic AGN contribution to the observed total light (f_{AGN}).

Methods. We trained a deep learning (DL) based method Zoobot to estimate the fractional contribution of a central point source to the total light. Our training sample comprises realistic mock JWST images of simulated galaxies from the IllustrisTNG cosmological hydrodynamical simulations. We injected different amounts of the real JWST point spread function (PSF) models to represent galaxies with different levels of AGN contribution. Galaxies in our training sample span a wide range of morphologies, including merging galaxies. We analyse in detail the performance of our method as a function of various galaxy properties and compare it with results obtained from the traditional light profile fitting tool GALFIT.

Results. We find excellent performance of our DL method in recovering the injected AGN fraction f_{AGN} , both in terms of precision and accuracy. The mean difference between the predicted and true injected f_{AGN} is -0.0006 and the overall root mean square error (RMSE) is 0.027. The relative absolute error (RAE) is 0.086 and the outlier (defined as predictions with RAE $> 20\%$) fraction is 7.8%. In comparison, using GALFIT on the same dataset, we achieve a mean difference of -0.024 , RMSE of 0.09, RAE of 0.19 and outlier fraction of 19%. We also investigate quantitatively how these key performance metrics obtained from Zoobot and GALFIT vary as a function of the injected f_{AGN} , redshift, signal-to-noise ratio, and magnitude. In addition to superior performance, our DL method has several other advantages over traditional methods, e.g. it has a much higher success rate (even for highly disturbed or irregular galaxies) and is extremely fast and easy to use. In summary, our DL-based method to identify AGNs and estimate AGN contribution to the total light has a huge potential in future applications to large galaxy imaging surveys.

Key words. Galaxies: interactions – Galaxies: active – Galaxies: evolution – Techniques: image processing

1. Introduction

It is generally accepted that there exists co-evolution between supermassive black holes (SMBH) and their host galaxies (Kormendy & Ho 2013). One manifestation of this co-evolution is the tight correlation between the mass of an SMBH and its host galaxy properties, such as the stellar velocity dispersion, bulge luminosity and bulge mass (Gültekin et al. 2009; Beifiori et al. 2012; Graham & Scott 2013; McConnell & Ma 2013; Läsker et al. 2014). These correlations may hint at a fundamental connection between the central SMBH and the formation and evolution of its host galaxy. Theoretical models show that SMBH feedback, via radiative heating, outflows, or jets could potentially explain these correlations, by regulating or halting the growth of itself and the host galaxy (e.g., Somerville et al. 2008; Booth & Schaye 2009; Weinberger et al. 2018; Davé et al. 2019). However, these correlations could also arise from merging events, in which mergers could explain, for example, the growth of SMBH mass and the stellar mass of the host galaxy (e.g., Croton 2006; Peng 2007; Hirschmann et al. 2010; Jahnke & Macciò 2011). To better understand the co-evolution (or not)

of SMBHs and host galaxies, it is important to study their link at different cosmic times. At high redshifts, studies have to rely on accreting SMBHs, which are active galactic nuclei (AGNs), to be able to obtain SMBH mass estimates, and in particular Type I AGNs. It is also necessary to obtain quantitative measures of the physical properties of the host galaxies. However, the presence of a bright central AGN can make this task very difficult, particularly for the bulge component, as galaxies with significant contribution from the AGN to the total flux will appear more bulge-dominated (Pierce et al. 2010).

It is crucial to correctly separate the central AGN light from the host galaxy, across a wide range of galaxy types and redshifts. Good quality optical imaging, with high spatial resolution and signal-to-noise, is needed to decompose the observed total light into contributions from the host galaxy and the central AGN. Traditionally, this is done in photometric data by fitting two-dimensional (2D) profiles to the galaxy's light, using one (or more if needed) analytic profile to describe the galaxy (typically a Sérsic profile) and a point spread function (PSF) profile to describe the central point source. Many studies use GALFIT (Peng et al. 2002), one of the most widely used 2D surface brightness modelling software to perform image-based

* e-mail: B.Margalef.Bentabol@sron.nl

decomposition of AGN and host galaxy light (e.g. [Kim et al. 2008](#); [Bentz et al. 2009](#); [Gabor et al. 2009](#); [Böhm et al. 2013](#); [Schramm & Silverman 2013](#); [Du et al. 2014](#); [Urbano-Mayorgas et al. 2019](#); [Son et al. 2022](#); [Aird et al. 2022](#); [Ji et al. 2022](#); [Dewsnup et al. 2023](#); [Zhuang & Ho 2023](#); [Sturm & Reines 2024](#); [Zhuang et al. 2024](#)). However, there are some known technical issues with GALFIT. For example, in certain circumstances, particularly for extremely compact sources, the minimisation algorithm used can be trapped in a local minimum. Other software have been used in an attempt to improve on GALFIT performance, such as PSFMC ([Mechtley 2014](#)), which is a Markov Chain Monte Carlo (MCMC) simultaneous fitting software to perform multi-component profile fitting ([Mechtley et al. 2016](#); [Marshall et al. 2021](#)) and LENSTRONOMY ([Birrer et al. 2015](#); [Birrer & Amara 2018](#)), which uses particle swarm optimisation ([Kennedy & Eberhart 1995](#)) for χ^2 minimisation, to reduce the likelihood of getting trapped in a local minimum when searching the parameter space, and MCMC for Bayesian parameter inference ([Foreman-Mackey et al. 2013](#)). The latter method is used by ([Li et al. 2021](#)) to decompose a sample of X-ray selected AGNs into quasars and host galaxy components, to investigate the properties of the host galaxies. However, these approaches all assume that the galaxy's surface brightness profile can be well fitted by a single Sérsic profile (or combination of Sérsic profiles), which may not be the case, particularly for irregular galaxies, highly disturbed merging galaxies, or galaxies with complicated substructures.

Consequently, if Sérsic profiles cannot adequately describe the host galaxy light, it can introduce a systematic bias in the derived luminosity of the PSF component and of the host galaxy. In addition, if there is a significant contribution to the total flux from the central AGN, it can lead to a bias in the morphology of the host galaxy, as it may appear more bulge-dominated ([Pierce et al. 2010](#)). Indeed, it is not always a good idea to represent a galaxy with a single Sérsic profile. [Bentz et al. \(2009\)](#) study AGN host galaxies at redshift $z \approx 0.7$, by fitting their surface brightness distributions with a combination of Sérsic profiles (to account for the host galaxy's light) and PSF profile (to describe the AGN component). They find that most galaxies in their sample are well described with two Sérsic profiles, in addition to the PSF profile, and a few of them required three or more Sérsic profiles to describe additional components such as bars. Another possible difficulty in decomposing the AGN from the host galaxy is the (sometimes significant) variation of the PSF in a given survey due to spatial/temporal changes or differences in galaxy spectral energy distributions (SEDs), as an incorrect PSF can bias the estimated contribution of the AGN to the total flux of the galaxy. [Kim et al. \(2008\)](#) perform 2D decomposition of Sérsic + PSF profiles to galaxies hosting AGNs in *Hubble Space Telescope* (HST) images and investigates the effect of realistic PSF mismatch, finding a systematic overestimation of the flux of the host galaxies, particularly for those containing bright AGNs.

Without additional information on the possible presence of AGN activity in a galaxy (e.g., from X-ray, mid-infrared or radio observations), it is not always easy to discern whether a galaxy has an AGN component in the form of a central point source from 2D surface brightness fitting, particularly for galaxies with very concentrated light profiles. This is because galaxy light in some cases could be more or less equally well described by a single Sérsic component or a combination of Sérsic + PSF profiles. A more complex model will always have a smaller χ^2 . Therefore, a better fit is not a necessarily good indicator to decide between different models. To mitigate this problem, [Aird et al. \(2022\)](#) fits the *HST* imaging of a sample of galaxies in the Cosmic As-

sembly Near-infrared Deep Extragalactic Legacy Survey (CANDELS; [Koekemoer et al. 2011](#); [Grogin et al. 2011](#)) at $z = 0.5 - 3$ with a Sérsic profile plus an additional central point source component and with a Sérsic profile only, and then used the residual flux fraction (RFF; [Hoyos et al. 2011](#)) to determine which is the best model. The RFF measures the fraction of the flux contained in the residual image that cannot be explained by fluctuations in the background. However, good estimates of the background and galaxy's size are needed for this method.

In this work, we present a promising new methodology to determine the AGN contribution to the total flux of a galaxy in imaging data, by combining deep learning (DL) methods and cosmological hydro-dynamical simulations. Over the last decade or so, DL methods have been widely used for diverse astronomy applications ([Dieleman et al. 2015](#); [Huertas-Company et al. 2018](#); [Walmsley et al. 2020](#); [Margalef-Bentabol et al. 2020](#); [Zanisi et al. 2021](#); [Huertas-Company & Lanusse 2023](#)). In particular, they show great success in different image-based astronomical problems, such as morphological classifications of galaxies (e.g., [Huertas-Company et al. 2015](#); [Domínguez Sánchez et al. 2018](#); [Cheng et al. 2020](#); [Walmsley et al. 2022a](#)), merger identifications ([Bottrell et al. 2019](#); [Ferreira et al. 2020](#); [Cíprjanović et al. 2020](#); [Pearson et al. 2022](#); [Bickley et al. 2021](#); [Margalef-Bentabol et al. 2024](#)) and determining galaxy physical properties and structural parameters ([Tuccillo et al. 2018](#); [Simet et al. 2021](#); [Euclid Collaboration et al. 2023](#)). On the other hand, the use of cosmological hydro-dynamical simulations allows us to create a comprehensive training sample of diverse and realistic galaxies, spanning a large range in redshift and mass.

Our DL model is trained on mock images of simulated galaxies with different levels of AGN contributions to the total flux. The construction of our training sample can easily incorporate the full information on the expected variations of the PSF. Therefore, our DL model can learn to infer the intrinsic AGN fraction automatically folding in the impact of different PSFs. In comparison, while it is possible to examine the goodness-of-fit for different PSF models for methods based on light profile fitting such as GALFIT, in practice it will be extremely time-consuming, particularly for large samples of galaxies. Another advantage of our DL-based method is that it does not rely on an assumed (and often simplified) galaxy surface brightness profile which in many cases is not able to fully describe a galaxy's light profile and thus can introduce biases in the estimation of the AGN contribution. Finally, our method, like any other machine learning-based method, has the advantage of being very fast to implement in new data once the DL model has been trained, making it much more computationally efficient than any traditional method based on light profile fitting.

This paper is organised as follows. In Section 2, we describe the observed *James Webb Space Telescope* (JWST; [Gardner et al. 2006](#)) imaging data used in this work and the generation of the corresponding mock JWST images of simulated galaxies selected from the IllustrisTNG. Of particular importance are the real JWST PSF models and their variations within the survey data. In Section 3, first we explain how we create the final images mimicking galaxies containing AGNs by injecting different levels of PSF contribution (taken as AGN contribution) to mock JWST images. Then we introduce our DL-based method (Zoobot; [Walmsley et al. 2023](#)) to recover the intrinsic AGN fraction in the observed total light. To compare with traditional light profile fitting-based methods, we also briefly describe GALFIT and how we use it in this work. In Section 4, we present in detail the results from both methods and compare their performances as a function of various galaxy properties.

Finally, in Section 5 we summarise the paper and highlight the main conclusions of our work. Throughout the paper we assume a flat Λ CDM universe with $\Omega_M = 0.2865$, $\Omega_\Lambda = 0.7135$, and $H_0 = 69.32 \text{ km s}^{-1} \text{ Mpc}^{-1}$ (Hinshaw et al. 2013). Unless otherwise stated, magnitudes are presented in the AB system.

2. Data

In this section, we first introduce the real JWST observations and the PSF models obtained from the COSMOS-Web survey. Then, we describe the synthetic JWST images generated using simulated galaxies selected from the IllustrisTNG cosmological hydrodynamical simulations. The observed and simulated datasets are combined later to create mock galaxy JWST images with different levels of AGN contribution.

2.1. JWST/COSMOS-WEB

COSMOS-Web (Casey et al. 2023, PIs: Kartaltepe & Casey, ID=1727) is a 255-hour JWST treasury imaging survey observing the central area of the Cosmic Evolution Survey (COSMOS; Scoville et al. 2007) field which is one of the most popular deep multi-wavelength survey fields. It covers a contiguous 0.54 deg^2 region in four Near Infrared Camera (NIRCam) filters (F115W, F150W, F277W, and F444W), reaching a 5σ point source depth of $27.5 - 28.2$ magnitudes. In parallel, a 0.19 deg^2 area of Mid-Infrared Instrument (MIRI) imaging with the F770W filter is covered. For this work, we make use of the 0.28 deg^2 JWST/NIRCam F150W images reduced by Zhuang et al. (2024). They used version 1.10.2 of the JWST¹ pipeline with the Calibration Reference Data System (CRDS) version of 11.17.0. to reduce the uncalibrated NIRCam raw data retrieved from MAST². The steps followed in the data reduction process are briefly summarised in the following:

1. Individual exposures of raw data were reduced using the Stage 1 pipeline Detector1Pipeline, in which they used some custom parameters to better flag large cosmic ray events and snowballs.
2. Fully calibrated individual exposures were obtained from running the Stage 2 pipeline Image2Pipeline, which performed wcs assignments, flat-fielding and photometry calibration.
3. A two-dimensional background was subtracted, after masking bad pixels and sources using SextractorBackground in the photutils package (Bradley et al. 2024).
4. Wisps (artefacts caused by scattered light in the mirror) and claws (features caused by scattered light coming from extremely bright stars) were subtracted.
5. Finally, single mosaics for each filter were produced using the Stage 3 Image3Pipeline, by combining all calibrated images.

For each NIRCam mosaic, Zhuang et al. (2024) constructed three different PSF models. For this work, we used the global PSF models, which are produced using all of the point-like sources across the entire field-of-view (FoV) of each dither-combined mosaic. The median PSF full width at half maximum (FWHM) in the COSMOS-Web NIRCam mosaics is 61.1 mas for the F150W filter. The PSF in the NIRCam imaging has a fractional root mean square (RMS) temporal variation of PSF

FWHM of $\sim 2.4\%$ for F150W, which is dominated by short timescale fluctuation. In comparison, the spatial variation of PSF FWHM, dominated by random variations, is much larger, at a level of $\geq 5\%$ for short-wavelength filters including F150W. For a full description of their data reduction method, we refer the reader to Sect. 2.1 of Zhuang et al. (2024). The reduced NIRCam F150W imaging data as well as the PSF models used in this work are available at https://ariel.astro.illinois.edu/cosmos_web/. In Fig. 1 we illustrate the variations of the adopted global PSF models. We first stacked all 80 PSF models and then calculated the mean and the standard deviation pixel by pixel (displayed in the top and central panels of Fig. 1, respectively). The bottom panel of Fig. 1 shows the relative dispersion (or coefficient of variation), which is the standard deviation divided by the mean (pixel by pixel).

2.2. Mock JWST images

The IllustrisTNG project (Nelson et al. 2019; Pillepich et al. 2018; Springel et al. 2018; Nelson et al. 2018; Naiman et al. 2018; Marinacci et al. 2018) is a series of cosmological hydrodynamical simulations of galaxy formation and evolution, with three different runs that differ in volume and resolution. These runs are TNG50, TNG100, and TNG300, with comoving length sizes of 50, 100, and $300 \text{ Mpc } h^{-1}$, respectively. The initial conditions for all runs are drawn from Plank results (Planck Collaboration et al. 2016). For this work, we used TNG100 (better resolution than TNG300 but still with a big enough volume to contain a sufficiently large number of galaxies), which contains 1820^3 dark matter (DM) particles with a mass resolution of $M_{\text{DM, res}} = 7.5 \times 10^6 M_\odot$. In comparison, the baryonic particle resolution of TNG100 is $M_{\text{baryon res}} = 1.4 \times 10^6 M_\odot$. We refer the reader to Pillepich et al. (2018) for more details on IllustrisTNG.

In this work, we selected galaxies from six simulation snapshots (numbers 67, 64, 61, 58, 55 and 52), which correspond to redshifts from $z = 0.5$ out to 0.92. The time step between each snapshot is roughly ~ 480 Myr over this redshift interval. We selected all galaxies from these six snapshots with stellar mass $M_* > 10^9 M_\odot$ to ensure that most galaxies have a sufficient number of stellar particles (hence reasonably well resolved), with the lowest mass galaxies in TNG100 ($M_* = 10^9 M_\odot$) consisting of 714 particles. This selection in mass and redshift resulted in a total of ~ 120000 galaxies. Every galaxy in IllustrisTNG has a complete merger history available from applying the SUBLINK algorithm on baryon-based structures (Rodriguez-Gomez et al. 2015). We used these merger trees to identify major mergers and non-merger galaxies. Specifically, major mergers are defined as galaxies with stellar mass ratios $> 1:4$ and that will either have a merger event in the following 0.8 Gyr (pre-mergers) or had a merger event in the last 0.3 Gyr (post-mergers). Consequently, galaxies that do not satisfy these conditions are considered as non-mergers.

For each galaxy, we generated a synthetic JWST/NIRCam F150W observation from the simulations with the following steps:

- First, we created a smoothed 2D projected map (Rodriguez-Gomez et al. 2019; Martin et al. 2022) constructed from the contribution from all stars after passing them through the JWST/NIRCam F150W filter. These maps do not include a full radiative transfer treatment and therefore do not account for dust. The images were produced with the same pixel resolution as the real JWST observations ($0.03''/\text{pixel}$), and have a physical size of $50 \times 50 \text{ kpc}$.

¹ <https://jwst-pipeline.readthedocs.io/en/latest/>

² <https://archive.stsci.edu/doi/resolve/resolve.html?doi=10.17909/6btv-br09>

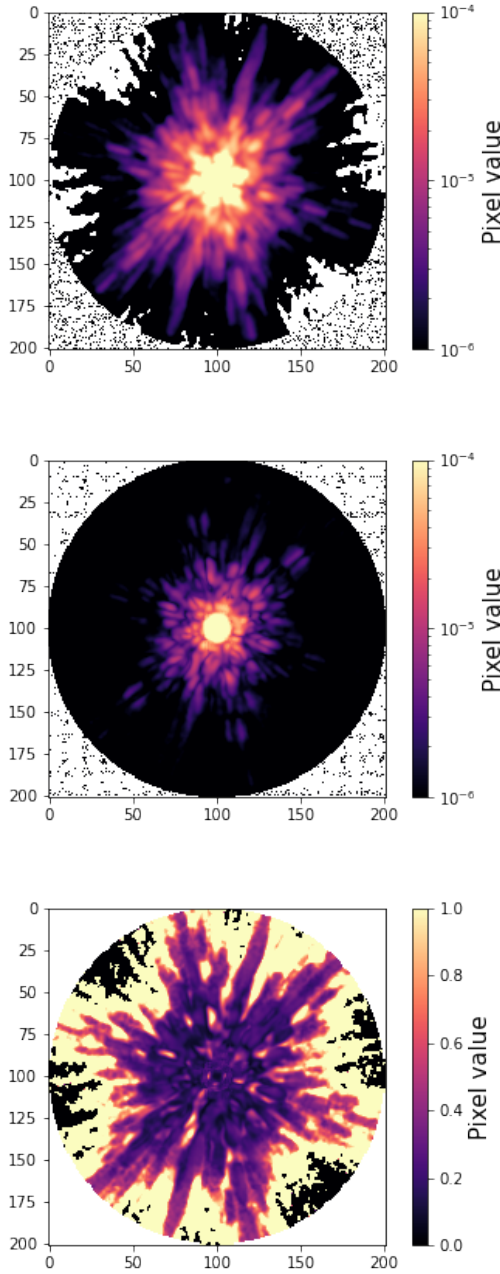


Fig. 1. Overview of the PSFs. We stacked all available PSFs from [Zhuang et al. \(2024\)](#) and show the mean PSF (top panel), standard deviation (central panel) and the coefficient of variation (bottom panel), calculated pixel by pixel. The pixel resolution is $0.015''/\text{pixel}$. The axes show the number of pixels, corresponding to $3''$. The colorbar shows the intensity of each pixel.

- Second, each image was convolved with a randomly chosen global JWST F150W PSF model (out of 80 in total, as derived by [Zhuang et al. 2024](#)). This step ensures that our training sample contains the full information on the (spatial and temporal) variation of the PSF.
- Third, Poisson noise was added to each image, to account for the statistical variation of a source’s photon emissions over time.

- Lastly, each image was injected into cutouts of real JWST F150W sky cutouts. This step ensures that fully realistic background and noise are included in our training data.

In the final step, we followed the same approach as in [Margalef-Bentabol et al. \(2024\)](#). To obtain cutouts of the real JWST sky, we first generated a catalogue of sources that we wanted to avoid within the central region of the cutouts. Starting from the ‘Farmer’ version of the COSMOS2020 catalogue ([Weaver et al. 2022](#)), we set the flag `FLAG_COMBINED` equal to 0 to select areas that are not affected by bright stars or large artefacts, as recommended by the COSMOS team. We then made use of the star/galaxy separation provided in the Le Phare photo- z , selecting sources with the star/galaxy flag `lp_type` equal to 0 (galaxy) or 2 (X-ray source). Finally, we restricted our selection only to $z < 3$ sources in the COSMOS-Web field. The final catalogue contains relatively bright sources, with average magnitudes being: HSC- $i = 25.6$ mag, UVISTA- $H = 24.7$ mag. Then, we generated random sky coordinates such that there are no catalogued bright sources within a circular radius of $6.5''$. This radius corresponds to the estimated source density of the area from which we extracted the cutouts. These criteria ensure that there are no bright sources in the centre of the cutouts, where the synthetic galaxies will be injected, but still allow for faint background galaxies. The random coordinates were then used as the centres for the sky cutouts, in which to inject the simulated galaxies, after performing sanity checks to ensure that no artefacts, stellar spikes, or bad or saturated pixels were present. For different snapshots of the simulation (and therefore, at different redshifts), a physical size of 50 kpc corresponds to a different image size in pixels (ranging from 210 to 270 pixels). To have a uniform dataset to train our deep learning model, we resized all images to 256 pixels. This transformation effectively changes the image pixel resolution depending on the corresponding snapshot/redshift, from $0.025''/\text{pixel}$ at the highest redshift to $0.032''/\text{pixel}$ at the lowest redshift. In Section 2.2, where we injected the observed PSF models, the pixel resolution of the PSF model was adjusted accordingly, to exactly match the pixel resolution of the mock images of simulated galaxies at different redshifts.

3. Methods

In this section, we first describe the construction of mock host galaxy images with different injected levels of AGN contribution. Then we introduce the two methods (our method based on DL and GALFIT based on 2D surface brightness fitting) used to estimate the AGN contribution.

3.1. Mock AGN injection

To simulate images of galaxies with AGNs, we injected a central point source into the host galaxy image. The observed JWST PSF models as described in Section 2.1 were used as the central point source. In order to create different AGN fractions, the relative brightness of the PSF was adjusted before injecting it into the mock JWST images described in Section 2.2.

The AGN fractions were chosen to range from 0.0 to 0.95 in increments of 0.05, for a total of 20 different AGN fractions. For any given AGN fraction f_{AGN} , the injected image was created as follows. First, the PSF image was transformed into the correct pixel scale for each redshift then, the flux of

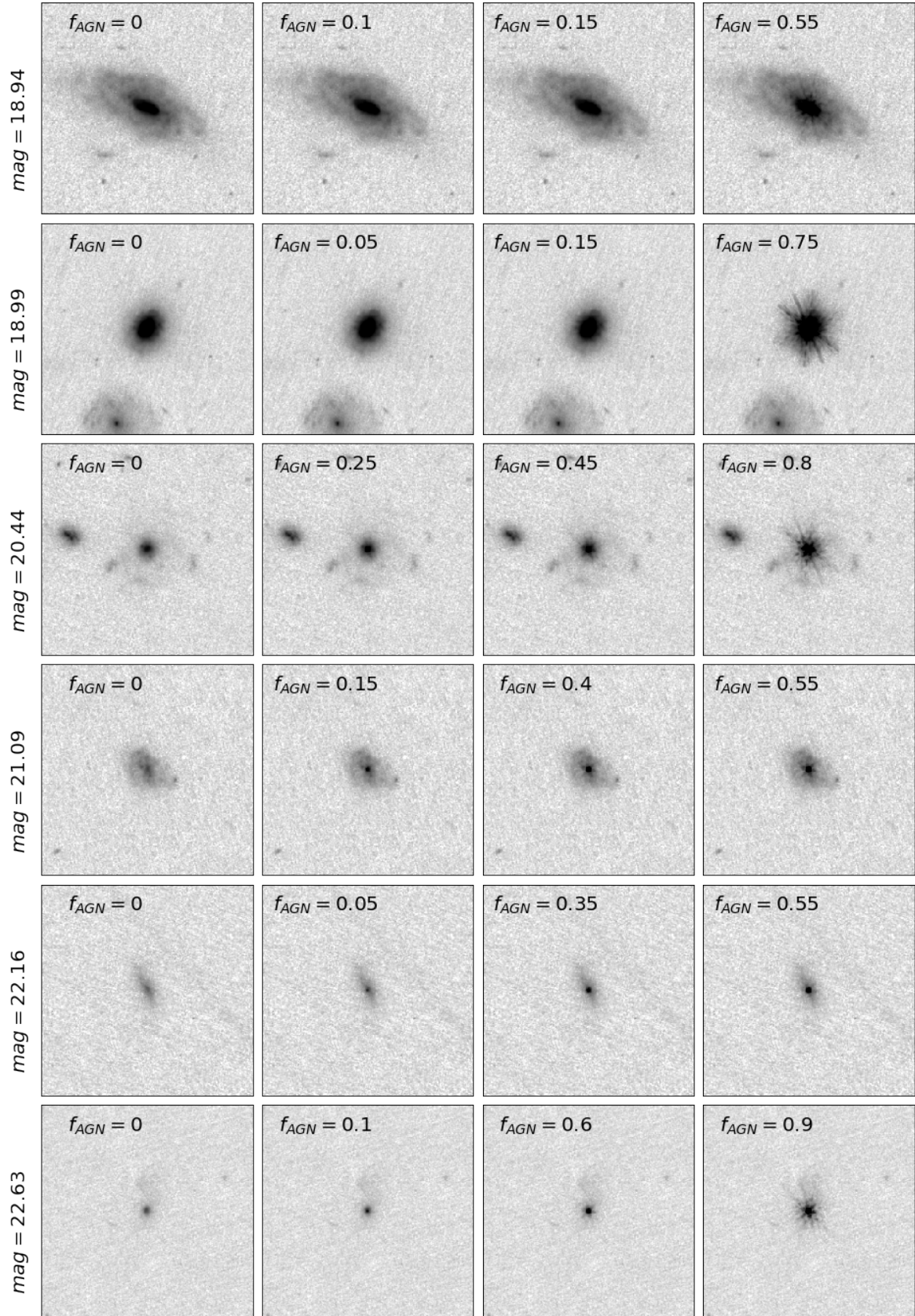


Fig. 2. Example mock JWST F150W images with varying levels of AGN contribution. The images have been generated to mimic JWST observations, and include realistic JWST noise and background. Each row corresponds to a different galaxy with no AGN contribution in the left panel and increasing AGN contributions in the rest of the panels. We show four example galaxies with different magnitudes, from the brightest (top) to the faintest (bottom). Images correspond to a physical size of 50 kpc and are displayed with an inverse arcsinh scaling.

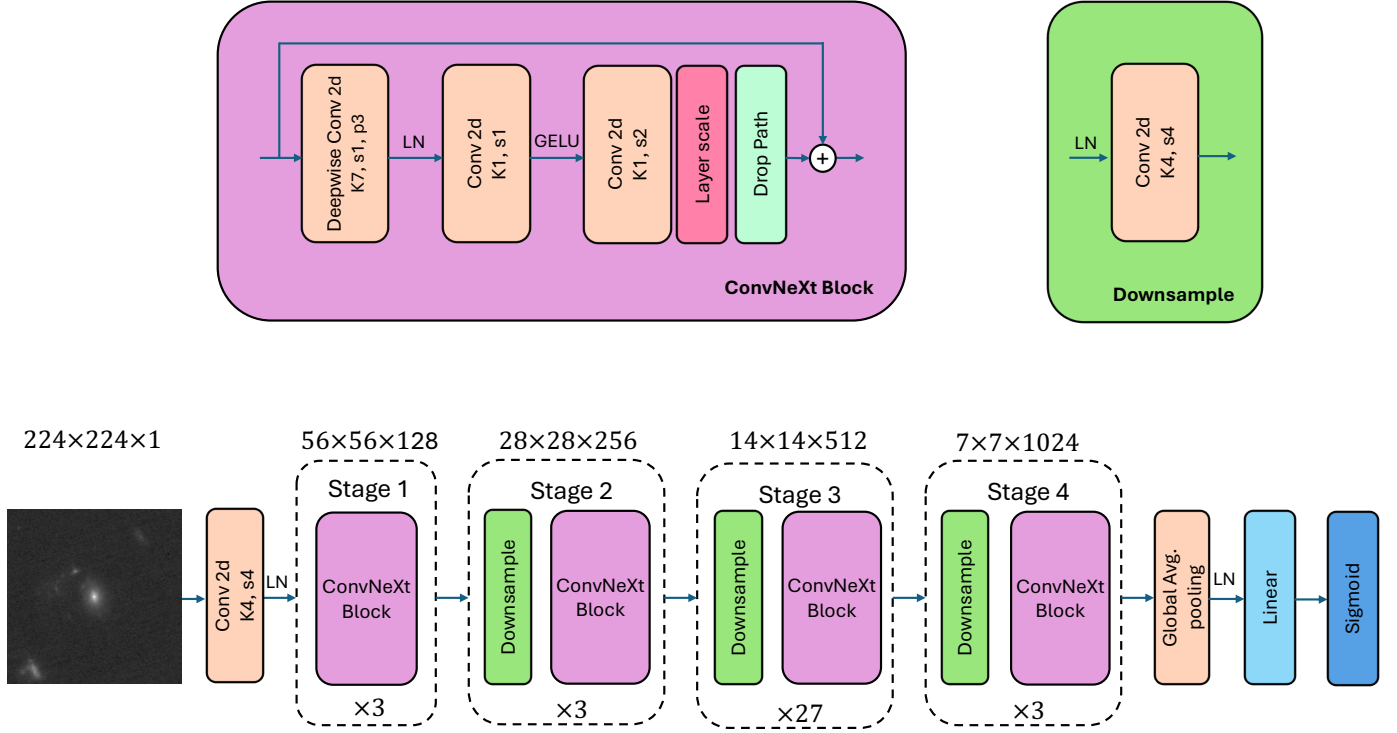


Fig. 3. Architecture of ConvNeXt-Base network (bottom) with a four-stage feature hierarchy, which allows us to extract features on different scales. On top of each stage, we show the dimension of the feature maps, with the width and height decreasing as the network deepens while the filter size increases. The top left diagram shows the internal structure of ConvNeXt Block. The top right diagram shows the internal structure of Downsample. The LN and GELU represent a layer normalisation and a Gaussian error linear unit activation function, respectively.

the PSF image was measured within a 3'' aperture³ using the `aperture_photometry` function of the `photutils` package (Bradley et al. 2024). This aperture size corresponds to sizes between 18.6 kpc and 23.9 kpc in our redshift range. The PSF image was normalised using this flux, so it could be easily adjusted later. The flux of the host galaxy image, F_{host} , was measured in the same way. The AGN fraction (i.e. contribution to the total light) is then defined as

$$f_{AGN} = \frac{F_{AGN}}{F_{host} + F_{AGN}}, \quad (1)$$

where F_{AGN} is the flux of the AGN. Afterwards, the normalised PSF image was multiplied by F_{AGN} , which can be derived from Equation 1:

$$F_{AGN} = \frac{f_{AGN}}{1 - f_{AGN}} F_{host}. \quad (2)$$

Finally, the transformed PSF image was added to the host galaxy image. For each galaxy, five different images were created with five different AGN fractions, chosen randomly from the 20 possible discrete AGN fractions. Some example images of these simulated galaxies (from bright to faint) with varying levels of AGN contributions can be seen in Fig. 2. Visually, it is clear that it can be very difficult to discern the presence of the host galaxy when $f_{AGN} \geq 0.8$, particularly for fainter and higher-redshift objects. Later we will examine how well we can quantify f_{AGN} as a function of redshift, magnitude, signal-to-noise, etc.

³ A 3 ''aperture corresponds to different sizes in pixels for different redshift, due to having resized all images to the same number of pixels.

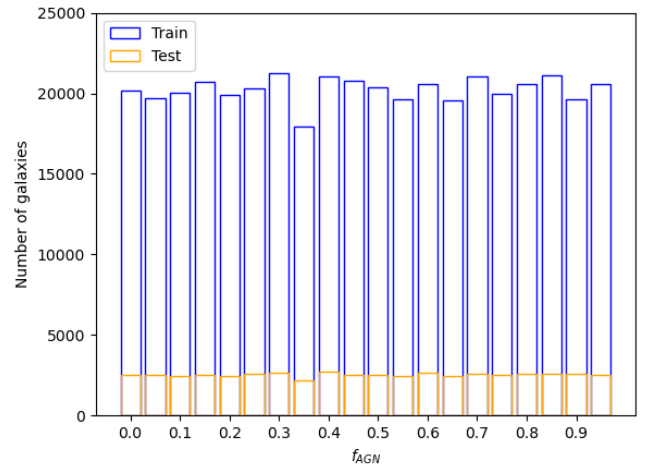


Fig. 4. Distribution of injected AGN fraction (as defined in Equation 1) in the training (blue) and test datasets (orange). The distributions are mostly uniform for the training and test datasets for the AGN fraction.

3.2. Deep learning CNN

Zoobot (Walmsley et al. 2023) is a Python package used to measure detailed morphologies of galaxies (such as spiral arms, bars and bulges) using DL based on the idea of successive layers of learned representations. Zoobot includes convolutional neural networks (CNNs, Fukushima 1988; LeCun et al. 2015) and vision transformer models (Dosovitskiy et al. 2021; Dehghani et al. 2023). These models are pre-trained on many millions of

labelled galaxies, derived from the visual classifications of the Galaxy Zoo project (Lintott et al. 2008) on real images of galaxies selected from surveys such as the Sloan Digital Sky Survey (SDSS), Hyper Suprime-Cam (HSC) and Hubble (Willett et al. 2013, 2017; Simmons et al. 2017; Walmsley et al. 2022a,b). The models are designed to be easily adaptable to new tasks (classification or regression tasks) and galaxy surveys with a minimal amount of new labelled data. Some of the available models in Zoobot belong to the family of ConvNeXts (Liu et al. 2022). They are pure convolutional models constructed by optimising the ResNet (He et al. 2015) architecture to bear resemblance with vision transformers (Vaswani et al. 2017; Liu et al. 2021), in which the design choices such as the use of the Gaussian Error Linear Unit (GELU) activation function or inverted bottleneck CNN blocks (which are a specialised type of residual block more computationally efficient than normal residual blocks) are proven to improve the performance of a purely CNN model and can compete with transformer in terms of accuracy and scalability. For this work, we chose a ConvNeXt-Base architecture, which was pre-trained on the Galaxy Zoo dataset of over 820k images and 100 million volunteer votes to morphological questions. In order to perform a regression task (as is the case in this study), we added a linear head with a sigmoid function (to restrict the output to be between 0 and 1) and used a mean square error loss function to train the network. A diagram of the ConvNeXt-Base network can be seen in Fig. 3. For this work, we retrained the last two blocks of the network and the linear head, while the rest of the network parameters were frozen to keep the optimal values found for the pre-trained data from Galaxy Zoo.

We split our sample of mock JWST images in training and test sets, with a 90/10 split. The distribution of the injected AGN fraction on the training and test datasets can be seen in Fig. 4. The training dataset was used for training Zoobot. A validation set of 10% of the training data was used to monitor the performance during training. The test set was used to determine the performance of the final model on data that had never been seen before by the algorithms. To ensure the test set cannot be learned by simply interpolating from the training set, the galaxies were split into the train, validation and test sets in a way that the five iterations of the same galaxy (with different injected AGN fractions) were only used in one of the splits. Furthermore, we randomly selected a subset of 2400 galaxies from the test set on which to directly compare the results from the DL methodology and surface brightness fitting with GALFIT. This subset was constructed in a way that for each snapshot we randomly selected 400 galaxies with a uniform distribution of f_{AGN} .

3.3. GALFIT

GALFIT (Peng et al. 2002) is a popular two-dimensional fitting code used to model the surface brightness of an object with pre-defined analytic functions. GALFIT allows the user to fit any number of components and different light profiles (e.g. Sérsic, exponential disk, PSF, etc.). The best-fit model is obtained by χ^2 -minimisation using a Levenberg-Marquardt algorithm. A Sérsic profile generally describes well the light distribution of spheroidal or disk galaxies (even though it will not be able to represent well disturbed or irregular galaxies). It has the following functional form,

$$\sum_e(R) = \sum_e \left\{ -\kappa_n \left[\left(\frac{R}{R_e} \right)^{1/n} - 1 \right] \right\}, \quad (3)$$

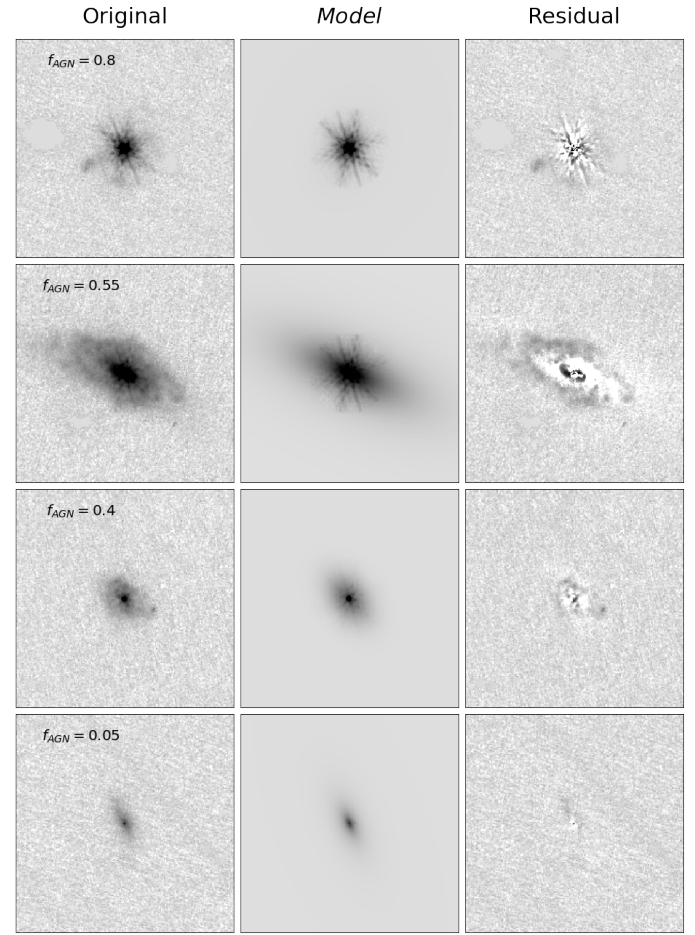


Fig. 5. Sérsic + PSF decomposition of four example galaxies (with AGN fraction varying from high to low from top to bottom) on which we performed GALFIT. Images of the original galaxy, the model (Sérsic + PSF), and the residual (original-model) are shown from left to right. Images correspond to a physical size of 50 kpc, and are displayed with an inverse arcsinh scaling.

where R_e is the effective radius, such that half of the total flux is contained within R_e , Σ_e is the surface brightness at R_e , n is the Sérsic index (it determines the shape of the light profile, and $n = 1$ represents a disk while $n = 4$ represents a spheroid), κ_n is a positive parameter that depends on n . On the other hand, the PSF profile can be used to describe a central point source such as the AGN. We can fit the surface brightness of each galaxy with a combination of Sérsic and PSF profiles in order to derive the contribution from a possible AGN component at the centre of the galaxy.

We ran GALFIT on the subset of 2400 galaxies from the test set. We first ran SExtractor (Bertin & Arnouts 1996) on all the test images to determine the central positions in pixels, x and y , the total magnitude of the galaxy, axis ratio (q) and effective radius (R_e). SExtractor also produces a segmentation map in which all galaxies are identified and can be used to either mask neighbouring galaxies or fit them simultaneously with the central galaxy. In order to perform χ^2 -minimisation, GALFIT requires a sigma map. This sigma map was constructed by adding the Poisson noise contribution from the simulated galaxy (after injecting the AGN contribution) to the error map provided by the JWST data.

We ran GALFIT with a combination of a single Sérsic profile and a PSF model for the main central galaxy in each image. Neighbouring galaxies were masked, unless their light overlaps with the central galaxy, in which case they were fitted simultaneously with a Sérsic profile. The initial estimates of the model parameters can have an impact on whether GALFIT finds a good fit or not. That is why we ran GALFIT with different initial parameters of Sérsic index and magnitudes. We chose the best model to be the one with the lowest reduced χ^2 . For the Sérsic index of the main galaxy, we chose as initial values $n = 1, 2, 4$, alternatively. For the magnitudes of the Sérsic and PSF models, we used three different combinations of the initial parameters. In the first scenario, both models were set to be equal to a magnitude that corresponds to half of the total flux obtained from SExtractor. In the other two scenarios, the magnitude of the PSF (Sérsic) model was set to be 80% of the total flux while the magnitude of the Sérsic (PSF) model was set to be 20%. For the rest of the parameters (position x and y, axis ratio, position angle and effective radius), we used as initial values those obtained by SExtractor. For the neighbouring galaxies that were fitted simultaneously, we also used the SExtractor parameters plus a Sérsic index of $n = 2$.

In some cases, GALFIT did not converge and did not produce a fit at all. In other cases, even if GALFIT produced an output, it was clearly not a good fit for the surface brightness light. We only selected galaxies for which GALFIT produced a good fit, that is, it has a reduced $\chi^2 < 5$ and no non-physical parameters (for example effective radius smaller than 0.5 pixels, or larger than the size of the image stamp, $q < 0.1$, and $n < 0.5$ or $n > 10$). In Fig. 5, we present good GALFIT fits of example galaxies containing varying amounts of injected AGN fractions (from insignificant to dominant AGN contributions), with the original image, the model image (Sérsic + PSF) and the residual image (original - model) shown in different columns. After the best fit had been found, we created images of each model separately (Sérsic and PSF) using the parameters from the best fit. We then calculated the flux within an aperture of 3'' in the Sérsic model, the PSF model and the original galaxy image.

Finally, we calculated the AGN fraction derived from running GALFIT in two slightly different ways. In the first method, we set the derived AGN fraction to be equal to the ratio of the aperture flux from the PSF component to the aperture flux of the original galaxy image (which corresponds to the total flux of the galaxy within a 3'' aperture). In the second method, we used as total flux (within a 3'' aperture) the sum of the aperture fluxes of the PSF and the Sérsic model. We adopted these two different approaches to calculating the total flux of the galaxy in order to understand if there is any systematic bias in the Sérsic model, which could also impact the flux of the PSF model.

4. Results

In this section, we first present results from our DL-based method Zoobot. We analyze in detail how key metrics such as the root mean square error (RMSE), relative absolute error (RAE) and outlier fraction vary as a function of the injected AGN fraction, redshift, signal-to-noise (S/N), and magnitude. Then we compare these results with the performance obtained from running GALFIT on the same test set.

4.1. Zoobot model performance

Here we analyse the performance of the Zoobot model on the subset of 2400 galaxies from the test set. We first calculate the

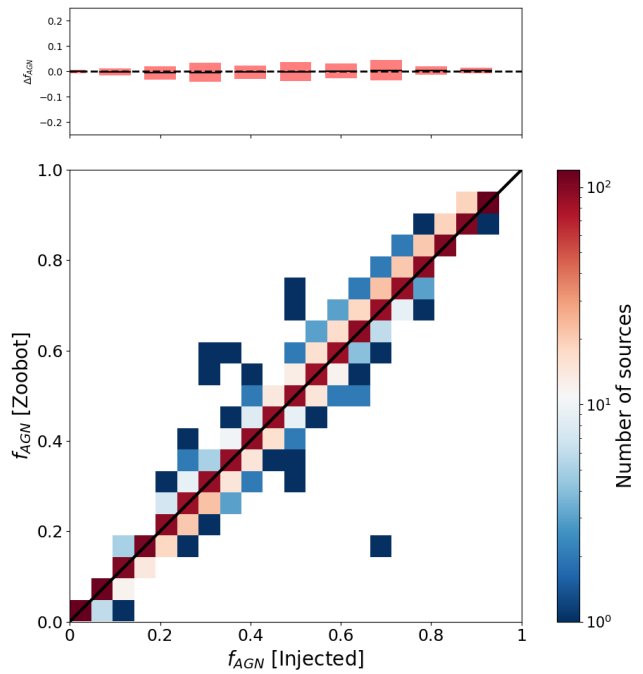


Fig. 6. Comparison between the real injected AGN fraction and the AGN fraction obtained from the Zoobot model on the subset of 2400 galaxies across the whole redshift range ($0.5 < z < 1$). The comparison shows a mean difference between the two quantities ($\Delta f_{AGN} = f_{AGN} [\text{Injected}] - f_{AGN} [\text{Zoobot}]$) of -0.0006 and an overall RMSE = 0.027. The solid diagonal line is the 1:1 line. The top plot shows the mean difference and its dispersion as a function of the injected AGN fraction. The colour bar indicates the number of sources in each 2D bin.

root mean square error (RMSE),

$$\text{RMSE} = \sqrt{\frac{1}{n} \sum_{i=1}^n (f_{AGN}^i [\text{injected}] - f_{AGN}^i [\text{predicted}])^2}, \quad (4)$$

which measures the average difference between the predicted values from a model (e.g. Zoobot or GALFIT) and the actual injected values. In Fig. 6 we show the predicted values of f_{AGN} , obtained from Zoobot, versus the real f_{AGN} for all redshifts, which shows a very tight correlation across the whole dynamic range. Quantitatively, we found an overall value of RMSE = 0.027 for the Zoobot model, demonstrating very good recovery (both in terms of accuracy and precision) of the injected real AGN fractions. In addition, the top panel of Fig. 6 shows the mean and the dispersion of the difference between the real and predicted values ($\Delta f_{AGN} = f_{AGN} [\text{injected}] - f_{AGN} [\text{Zoobot}]$) as a function of the injected AGN fraction, with a value for the mean of $\langle \Delta f_{AGN} \rangle = -0.0006$, and dispersion of $\sigma(\Delta f_{AGN}) = 0.027$. This shows that there is very little bias from the Zoobot predictions to the actual values, and it is independent of f_{AGN} , as the difference between the real and predicted value over the whole range of f_{AGN} is always below -0.006. Moreover, the overall dispersion is very small, particularly for the high and low injected AGN fractions ($f_{AGN} \gtrsim 0.8$ and $f_{AGN} \lesssim 0.2$). To check if the performance depends on galaxy structural properties, we further explore whether the Sérsic index impacts how well Zoobot can predict the AGN fraction (see Fig. A.1 in Appendix A) and find that for galaxies with $n < 1$ the RMSE increases by 30%, to RMSE = 0.035 and that high Sérsic indexes ($n > 1$) do not lead to worse predictions (RMSE = 0.020).

In Fig. 7 we show the RMSE of the Zoobot predictions (purple lines) as a function of the injected AGN fraction, redshift,

Table 1. Performance statistics for Zoobot and GALFIT.

| | RMSE | RAE | $\langle \Delta f_{AGN} \rangle$ | Outlier (20%) | Outlier (30%) |
|--|-------------------|-------------------|----------------------------------|-------------------|-------------------|
| Zoobot | 0.027 ± 0.005 | 0.086 ± 0.004 | -0.0006 ± 0.0005 | 0.078 ± 0.006 | 0.063 ± 0.005 |
| Zoobot ^M | 0.019 ± 0.004 | 0.085 ± 0.009 | -0.0021 ± 0.0008 | 0.07 ± 0.01 | 0.06 ± 0.01 |
| Zoobot ^{NM} | 0.029 ± 0.005 | 0.087 ± 0.005 | -0.0001 ± 0.0007 | 0.081 ± 0.007 | 0.064 ± 0.006 |
| GALFIT (f_{host} from original image) | 0.090 ± 0.008 | 0.19 ± 0.01 | -0.018 ± 0.002 | 0.19 ± 0.01 | 0.130 ± 0.009 |
| GALFIT ^M (f_{host} from original image) | 0.090 ± 0.009 | 0.27 ± 0.05 | -0.024 ± 0.004 | 0.25 ± 0.03 | 0.18 ± 0.02 |
| GALFIT ^{NM} (f_{host} from original image) | 0.090 ± 0.008 | 0.17 ± 0.01 | -0.016 ± 0.002 | 0.16 ± 0.01 | 0.113 ± 0.009 |
| GALFIT (f_{host} from model) | 0.141 ± 0.009 | 0.38 ± 0.02 | -0.072 ± 0.003 | 0.37 ± 0.02 | 0.27 ± 0.01 |
| GALFIT ^M (f_{host} from model) | 0.135 ± 0.008 | 0.44 ± 0.07 | -0.082 ± 0.005 | 0.47 ± 0.04 | 0.33 ± 0.03 |
| GALFIT ^{NM} (f_{host} from model) | 0.142 ± 0.008 | 0.36 ± 0.02 | -0.069 ± 0.003 | 0.34 ± 0.02 | 0.25 ± 0.01 |

Notes. We summarise the overall performance from Zoobot and GALFIT (for both ways of calculating the AGN fraction contribution), in terms of the RMSE, RAE, mean difference and outlier fractions (at different percentage levels, 20% and 30%). We show the results for the whole sample and mergers (M) and non-mergers (NM) separately.

signal-to-noise and magnitude (calculated in the F150W filter). The solid lines show the RMSE of the whole test subset. To separately investigate how the performance might change for highly disturbed or irregular galaxies, we also show galaxies classified as mergers (dashed lines) and galaxies classified as non-mergers (dotted lines), separately. In general, the RMSE is slightly lower for non-merging galaxies, but the difference with mergers is very small. We see that the RMSE is smaller for high and low values of the injected AGN fraction ($f_{AGN} \gtrsim 0.8$ and $f_{AGN} \lesssim 0.2$) and has a maximum mean value of 0.35 over the whole range of f_{AGN} . In fact at $f_{AGN} > 0.6$, for mergers, and $f_{AGN} > 0.4$, for non-mergers, Zoobots achieves smaller errors than the coefficient of variation of the PSF, that is, smaller error than the error on the PSF that results from the temporal and spatial variations (shaded region of Fig. 7). At intermediate levels of AGN contribution, the RMSE is a few times worse, perhaps indicating that image-based decomposition is harder when the brightness levels of the AGN and the host galaxy are comparable. There is a small increase of RMSE with increasing redshift, with a maximum value of RMSE = 0.043 at $z = 0.92$, possibly because galaxies at higher redshifts are smaller and tend to have lower signal-to-noise ratios (i.e. more dominated by noise). The latter is also observed when looking at the RMSE as a function of the signal-to-noise, where we see that the RMSE increases suddenly at $S/N < 10$. Finally, there is also an increase in the RMSE with increasing magnitude (i.e. towards fainter galaxies).

In Fig. 8 we show the relative absolute error (RAE), which is the ratio between the absolute error divided by the real value⁴,

$$RAE = \frac{|f_{AGN}[\text{injected}] - f_{AGN}[\text{predicted}]|}{f_{AGN}[\text{injected}]} \quad (5)$$

The purple lines (solid lines represent the whole test subset, dashed lines mergers and dotted lines non-merger) show the relative error from the Zoobot predictions as a function of the injected AGN fraction, redshift, signal-to-noise and magnitude (calculated in the F150W filter). We find that, while the RMSE decreases for low f_{AGN} , the relative error increases as f_{AGN} decreases, particularly for $f_{AGN} < 0.1$. While the RMSE only quantifies the absolute difference between real and predicted, the relative error does so in relation to the actual value. The relative error does not change with redshift. But, similarly to the RMSE, it increases with decreasing signal-to-noise and magnitude, as expected. Overall, there is a small difference between mergers

⁴ The relative error is not well defined when the real AGN fraction is equal to zero. In order to calculate the relative error when $f_{AGN}[\text{injected}] = 0$, we approximate it with $f_{AGN}[\text{injected}] = 1e-3$.

(dashed lines) and non-mergers (dotted lines), with non-mergers having slightly higher relative errors in some cases.

Finally, we explore the outlier fraction in the Zoobot predictions. Here we define outliers as the Zoobot predicted AGN fractions with an RAE of more than 20%, i.e.,

$$\frac{|f_{AGN}[\text{predicted}] - f_{AGN}[\text{injected}]|}{f_{AGN}[\text{injected}]} > 20\%. \quad (6)$$

In Fig. 9 we show the outlier fraction as a function of the injected AGN fraction, redshift, signal-to-noise and magnitude in purple lines. The overall outlier fraction for the whole sample is 7.8%. At intermediate to high levels of AGN contribution, the outlier fraction is extremely low (close to zero). However, at low levels of injected AGN fractions, particularly for $f_{AGN} < 0.1$, it increases very sharply with decreasing f_{AGN} . This behaviour is partly caused by our definition of outliers (i.e., it depends on whether we use a threshold on relative or absolute errors). The outlier fraction remains more or less constant as a function of redshift. Concerning the signal-to-noise ratio, there is only a small increase in the outlier fraction for $S/N < 10$. At $S/N > 10$, the outlier fraction drops to almost zero. As expected, there is a constant increase in the outlier fraction with decreasing magnitude. There is no significant difference in the outlier fractions between mergers (dashed lines) and non-mergers (dotted lines). In Table 1 we summarise the results obtained from Zoobot, in terms of the RMSE, RAE, mean difference and outlier fractions (at different percentage levels, 20% and 30%) for the whole test sample and for mergers and non-mergers separately.

4.2. GALFIT performance

We now analyse the results of the derived AGN fraction after performing 2D light profile fitting on the same subset as Sec. 4.1. Each galaxy was fitted with a single Sérsic and a PSF component, which describe the host galaxy and central source component, respectively. The AGN fraction derived from this method was calculated by dividing the flux (within a circular 3'' aperture) of the PSF model by the total flux of the galaxy (within the same aperture). As mentioned before, we can calculate the total flux in two ways: the first one is calculated from the original galaxy image (F_{Galaxy}) and the second one from the total model of the galaxy ($F_{\text{Sérsic}} + F_{\text{PSF}}$). We compare the two slightly different AGN fractions derived using GALFIT to better understand any possible bias introduced by fitting a Sérsic model.

In Fig. 10 we compare the AGN fraction obtained from running GALFIT (in the two ways explained above) with the

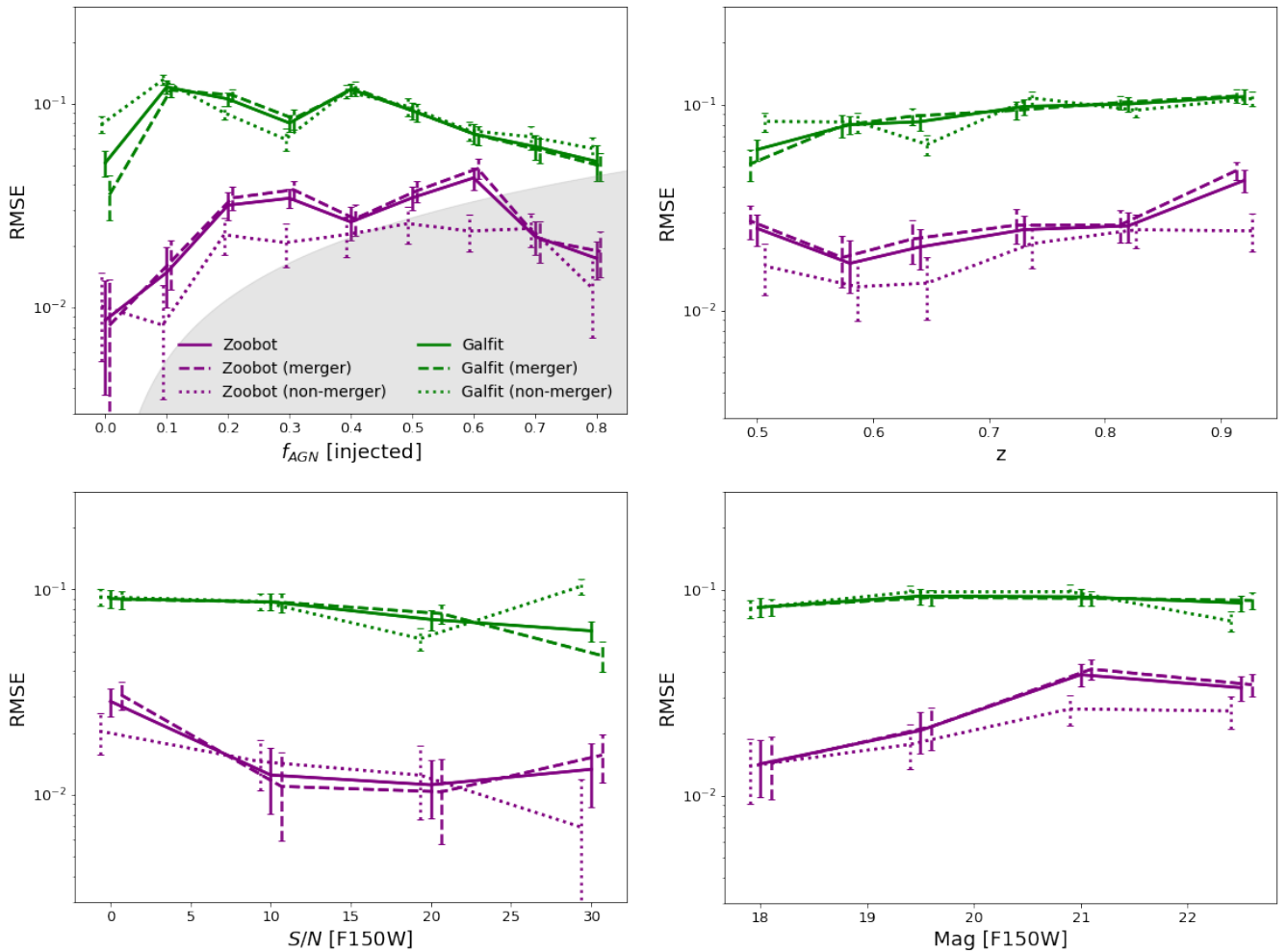


Fig. 7. RMSE as a function of the injected AGN fraction (top left panel), redshift (top right), signal-to-noise (bottom left) and magnitude (bottom right). The purple lines correspond to the results from Zoobot and the green lines from GALFIT. The solid lines correspond to the whole sample while the dashed and dotted lines correspond to the mergers and non-merger galaxies, respectively. The error bars show the 95% interval from bootstrapping the RMSE value. The performance of Zoobot is around a factor of 3 - 10 better than GALFIT. In general, highly disturbed or irregular galaxies such as mergers are more difficult for both methods. The shaded region on the top left panel represents the fractional variation (standard deviation divided by the mean) of the PSF, considering the spatial and temporal variations, showing how Zoobot is able to achieve smaller errors than the errors from the variation of the PSF.

real injected AGN fraction. When we calculate the AGN fraction by dividing by the total flux of the galaxy, we find that $\text{RMSE} = 0.090$, with a mean difference (between predicted and real value) of $\langle \Delta f_{\text{AGN}} \rangle = -0.018$ and dispersion: $\sigma(\Delta f_{\text{AGN}}) = 0.086$. However, when we consider the AGN fraction calculated completely from the model, we obtain slightly worse results, with $\text{RMSE} = 0.141$, $\langle \Delta f_{\text{AGN}} \rangle = -0.072$ and $\sigma(\Delta f_{\text{AGN}}) = 0.121$. This highlights how an inaccurate Sérsic model can bias the recovered AGN fraction. From now on, we only show the results from calculating the total flux of the galaxy from the original galaxy image. The RMSE obtained from GALFIT is more than three times higher than that obtained from Zoobot. There seems to be a small systematic offset (as seen by the mean difference) that is not found in the Zoobot results, and a larger spread between predicted and real (injected) AGN fractions than from Zoobot. In terms of dependence on galaxy structural properties, we find that galaxies with $n < 1$, have an increased RMSE of 47%, and it is even higher when the injected AGN fraction is small ($f_{\text{AGN}} < 0.2$), which means that GALFIT results are more affected by low Sérsic index than our deep learning methods. We do not see a worse prediction of the f_{AGN} for galaxies with high

Sérsic index for either method (see Fig. A.2 in Appendix A for more details on the effect of Sérsic index in predicting f_{AGN}).

Figures 7, 8 and 9 show the RMSE, relative error and outlier fractions, respectively, as defined in the previous Section. The green lines show the results from the AGN fraction obtained from GALFIT fitting. We see similar trends to those from Zoobot, but with larger values. We see that over all the galaxy properties (f_{AGN} , redshift, S/N and magnitude), the RMSE is always higher for GALFIT than for Zoobot results. Similarly to the Zoobot results, we observe a small increase of RMSE with increasing redshift and with decreasing S/N. We also observe a general decrease of RMSE with increased AGN fractions, although the RMSE also decreases for $f_{\text{AGN}} < 0.1$. This decrease for very low AGN fractions seems to arise due to the real AGN fraction value being very small. Actually, when looking at how the RAE changes with AGN fraction (Fig. 8) we see that it increases significantly as the AGN fraction decreases. The same results are observed with Zoobot, but again, the total RAE for GALFIT is higher than for Zoobot independently of AGN fraction, redshift, S/N or magnitude. Consequently, the outlier fraction is also always higher for GALFIT, with a dramatic increase,

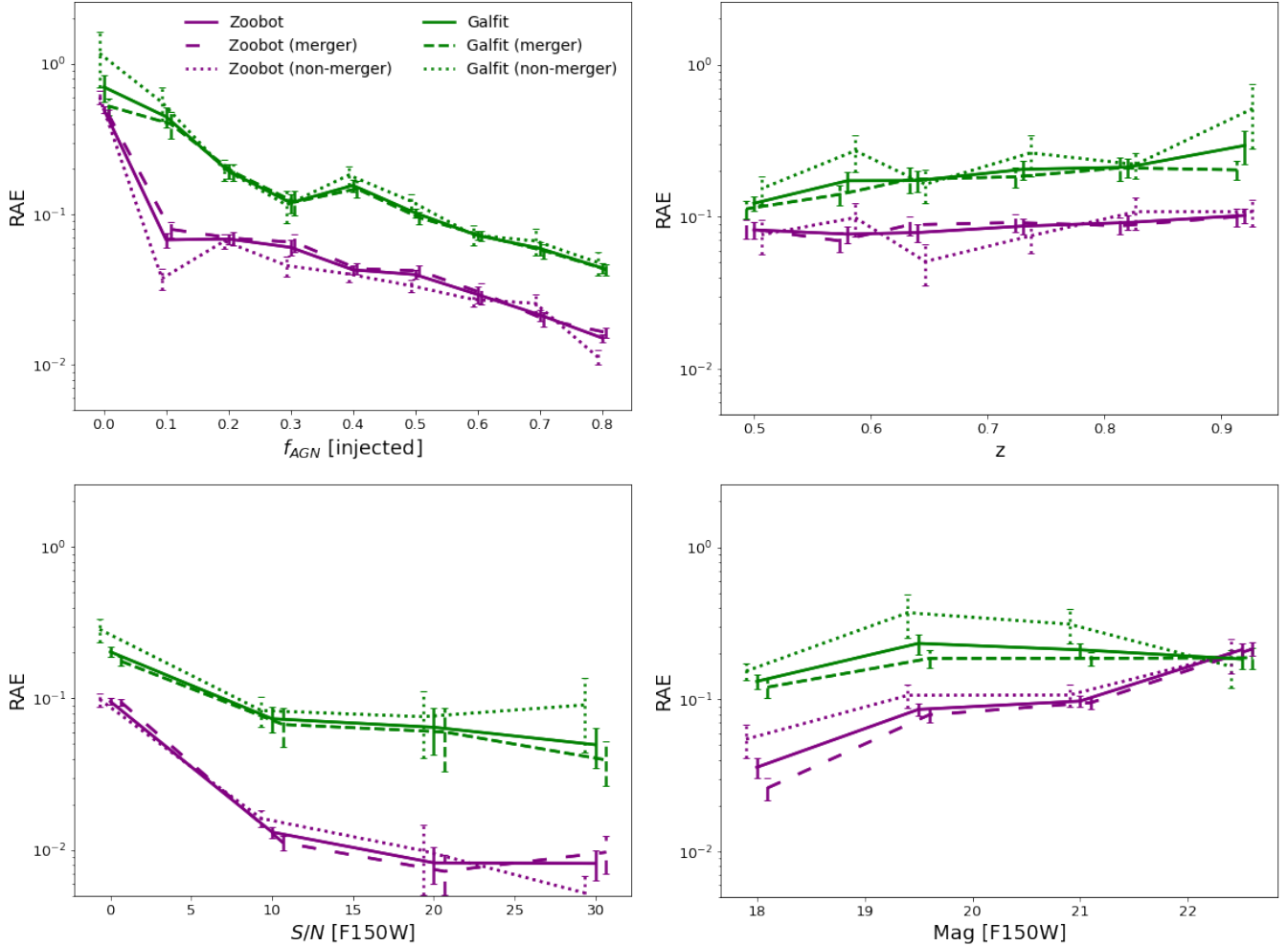


Fig. 8. Average relative absolute error in bins of injected f_{AGN} (top left panel), redshift (top right panel), signal-to-noise (bottom left panel) and magnitude (bottom right), from the Zoobot predictions. The error bars correspond to the standard deviation of the data points in each bin. The purple lines correspond to the results from Zoobot and the green, from GALFIT. The solid lines correspond to the whole sample while the dashed and dotted lines correspond to the merger and non-merger galaxies, respectively.

which was also observed in the previous Section, for $f_{AGN} < 0.2$. In Table 1, we summarise the results obtained from GALFIT, for the two ways to calculate the AGN fractions, that is, by either determining the total flux of the galaxy (within $3''$) from the original galaxy or the GALFIT model (Sérsic+PSF) and show the RMSE, RAE and outlier fractions (at different percentage levels, 20% and 30%) for the whole test sample.

We find that $19 \pm 1\%$ of all the galaxies from the subsample test set have no or bad fit from GALFIT. Furthermore, mergers are more likely to not have a good fit from GALFIT as expected, with $21 \pm 2\%$ of mergers having no or bad fits, and in particular, pre-mergers, for which GALFIT fails in $23 \pm 2\%$ of the cases, compared to non-mergers, in which $17 \pm 1\%$ of such galaxies have no or bad fits. In Fig. 11 we show that GALFIT fails more often for galaxies with high or low AGN fraction ($f_{AGN} \gtrsim 0.8$ and $f_{AGN} \lesssim 0.2$), higher redshift, lower signal-to-noise and very bright or faint galaxies. Therefore, even though we have previously seen that both the RMSE and RAE are relatively low for $f_{AGN} \gtrsim 0.8$, GALFIT fails to find a good fit in that regime for $44 \pm 4\%$ of the galaxies, while for $f_{AGN} \lesssim 0.2$ GALFIT fails for $18 \pm 2\%$ of galaxies. GALFIT also fails more often at the highest redshift bin ($23 \pm 3\%$ of fails), compared to $15 \pm 1\%$ for the rest of the sample, and $14 \pm 2\%$ for the lowest redshift bin.

Finally, GALFIT is more likely to fail for faint galaxies (with low signal-to-noise) and for very bright ones (with high signal-to-noise). There are $42 \pm 3\%$ of galaxies with no good fit for $mag > 23$ and $50 \pm 4\%$ for $mag < 19$. These results highlight the importance of good-quality images in order to find a good fit to the galaxy's light with GALFIT, while our deep learning methods can always determine a galaxy's AGN fractions with good accuracy and precision regardless of these galaxies' properties.

5. Summary and Conclusions

In this paper, we presented a new method to determine the AGN contribution to the total flux of a galaxy, based on DL methods and cosmological hydrodynamical simulations. We constructed the training sample for our DL model from the IllustrisTNG simulations. First, we mimicked the observational effects of JWST/COSMOS-WEB in the F150W filter, by using the same pixel scale, convolving with survey PSFs, adding Poisson noise and finally, adding real JWST background. Then, we artificially added an AGN component (approximated by the PSF) at different levels to represent different AGN contributions to the total flux. After training our model we analysed the results in detail on a test sample. Furthermore, we used GALFIT to fit the light

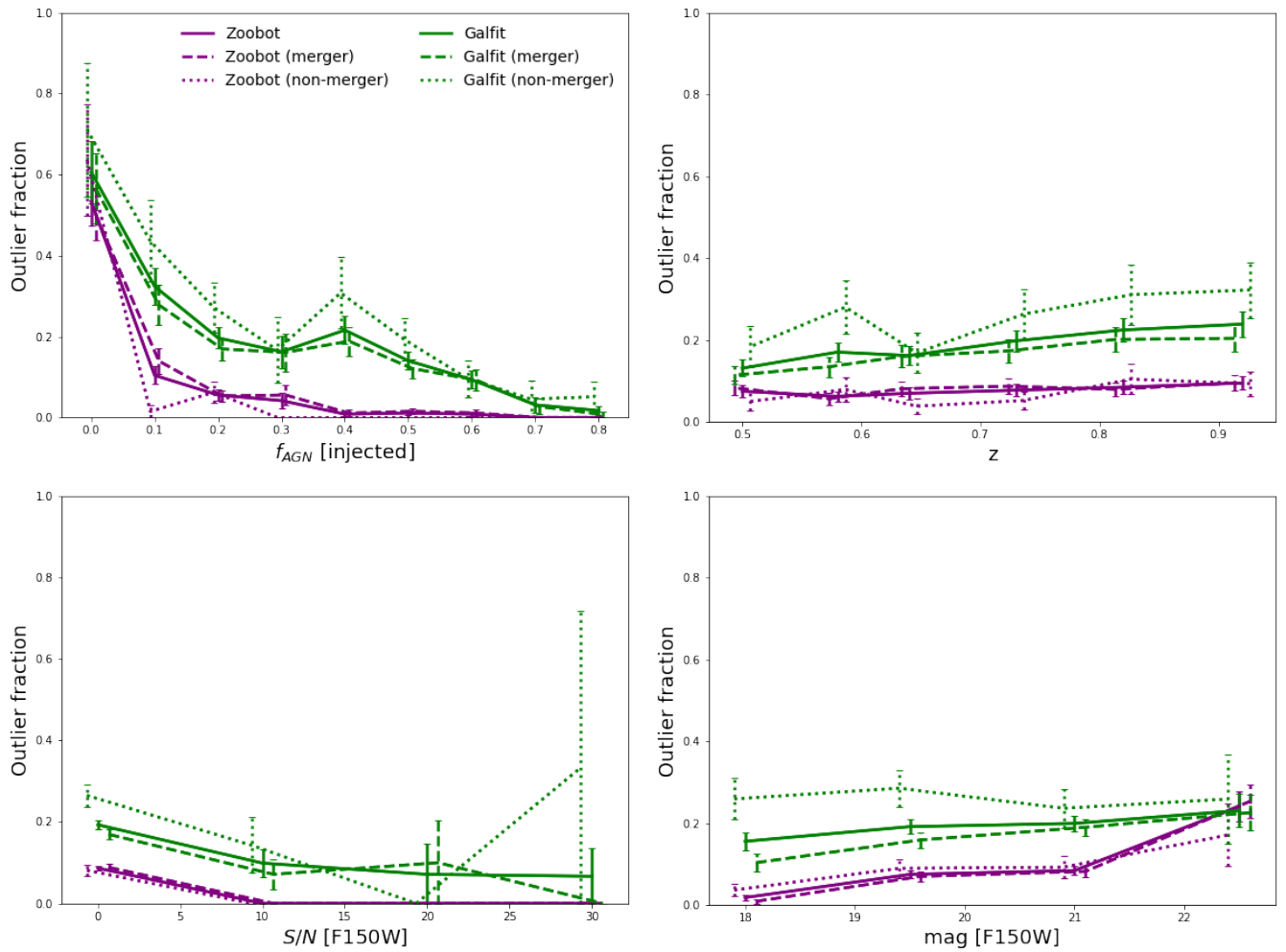


Fig. 9. Outlier fraction (calculated as the fraction of galaxies with RAE $> 20\%$) as a function of the injected AGN fraction (top left panel), redshift (top right), signal-to-noise ratio (bottom left) and magnitude (bottom right). The purple lines correspond to the results from Zoobot and the green, from GALFIT. The solid lines correspond to the whole sample while the dashed and dotted lines correspond to the merger and non-merger galaxies, respectively.

profile of the galaxies in the test sample with a combination of Sérsic + PSF profiles to calculate the AGN contribution within a circular aperture. We showed how our DL method outperforms the traditional 2D surface brightness fitting method. Our main results are summarised in the following:

- i) The f_{AGN} predicted by Zoobot has a very tight correlation with the injected f_{AGN} , with a mean difference of -0.0006 and an overall RMSE = 0.027 for the whole test sample, demonstrating how well our DL method is at recovering the true AGN contribution to the total flux. This performance metric is three times better than that obtained using GALFIT. In both methods, there is a decrease in the RMSE at low and high f_{AGN} . However, the low RMSE at $f_{AGN} \lesssim 0.2$ is, in part, a natural consequence of very small values of the true/injected f_{AGN} . In both methods, we see an increase in RMSE as redshift increases. While for Zoobot results the RMSE increases towards low S/N and high magnitudes, that is not the case for GALFIT, for which the RMSE remains roughly constant as a function of S/N and magnitude.
- ii) The outlier fraction given by Zoobot, as measured by the number of galaxies that have RAE $> 20\%$, is below 8% for most of the sample, except for galaxies with very low AGN fractions ($f_{AGN} < 0.1$) and faint galaxies (mag > 22).

There is only a small increase with magnitude and lower S/N. However, the outlier fraction is most affected by the AGN fractions and starts to increase for $f_{AGN} < 0.2$. The outlier fraction that we obtain from the GALFIT results is on average around 20%, and similarly to our Zoobot results, there is an increase with decreasing f_{AGN} , S/N and increasing magnitude. Furthermore, there is a small increase in the outlier fraction at higher redshift, which is not observed in the Zoobot results.

- iii) In constructing the training sample for our DL model, we fully incorporated the temporal and spatial variations of the PSF, which helps our model to better determine the intrinsic AGN fraction. And once it is trained our DL model can be easily applied to new data, without the need for user inputs as 2D fitting codes (such as GALFIT) do. Furthermore, it can output f_{AGN} predictions of thousands of galaxies in a few seconds, making it an ideal method for large extra-galactic imaging surveys.

In future works, we will study how AGNs selected via other methods, such as via X-ray, mid-infrared, or radio observations, compare with AGNs identified using our DL method. We can investigate in detail what is the f_{AGN} distribution of the X-ray/mid-infrared/radio-selected AGNs. A follow-up and complementary

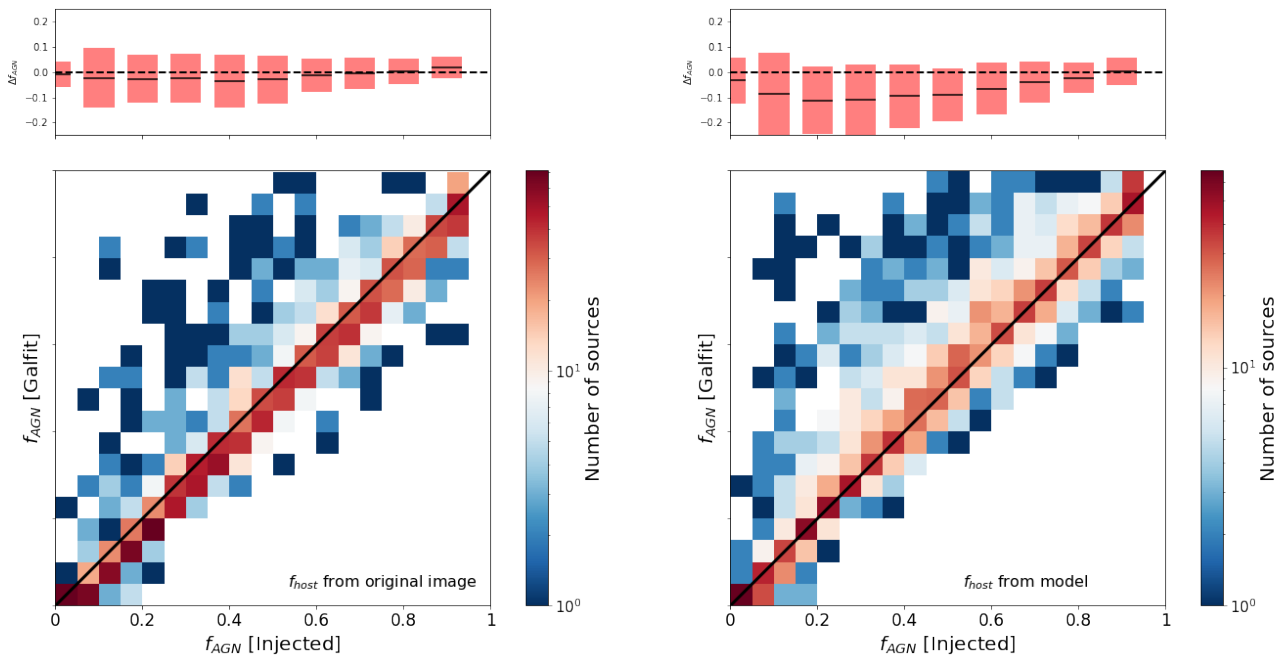


Fig. 10. Comparison between the real injected AGN fraction and the AGN fraction obtained from GALFIT fitting, obtained by dividing the PSF flux by the total flux. In the left panel, the total flux corresponds to the flux measured within a 3'' aperture in the original image, while in the right panel, the flux is measured within a 3'' aperture in the model (Sérsic+PSF). In both cases, the PSF flux is measured within the same aperture in the model PSF image. The dispersion in the left panel corresponds to $RMS E = 0.119$, and in the right, $RMS E = 0.138$. The colour bar provides the number of sources in each 2D bin.

approach that we also aim to develop in the near future will focus on not only inferring the level of AGN contribution to the observed total light but also decomposing the observed images into a pure AGN component and a host galaxy component. This will allow us to be able to investigate host galaxies of AGNs in more detail. For example, we can look for the presence of merging signs and bar features which could trigger AGNs.

Acknowledgements

This publication is part of the project ‘Clash of the Titans: deciphering the enigmatic role of cosmic collisions’ (with project number VI.Vidi.193.113 of the research programme Vidi which is (partly) financed by the Dutch Research Council (NWO). We thank the Center for Information Technology of the University of Groningen for their support and for providing access to the Hárrok high-performance computing cluster. We thank SURF (www.surf.nl) for the support in using the National Supercomputer Snellius.

References

Aird, J., Coil, A. L., & Kocevski, D. D. 2022, MNRAS, 515, 4860
 Beifiori, A., Courteau, S., Corsini, E. M., & Zhu, Y. 2012, MNRAS, 419, 2497
 Bentz, M. C., Peterson, B. M., Netzer, H., Pogge, R. W., & Vestergaard, M. 2009, ApJ, 697, 160
 Bertin, E. & Arnouts, S. 1996, A&AS, 117, 393
 Bickley, R. W., Bottrell, C., Hani, M. H., et al. 2021, MNRAS, 504, 372
 Birrer, S. & Amara, A. 2018, Physics of the Dark Universe, 22, 189
 Birrer, S., Amara, A., & Refregier, A. 2015, ApJ, 813, 102
 Böhm, A., Wisotzki, L., Bell, E. F., et al. 2013, A&A, 549, A46
 Booth, C. M. & Schaye, J. 2009, in American Institute of Physics Conference Series, Vol. 1201, The Monster’s Fiery Breath: Feedback in Galaxies, Groups, and Clusters, ed. S. Heinz & E. Wilcots (AIP), 21–24
 Bottrell, C., Hani, M. H., Teimoorinia, H., et al. 2019, MNRAS, 490, 5390
 Bradley, L., Sipócz, B., Robitaille, T., et al. 2024, astropy/photutils: 1.12.0

Casey, C. M., Kartaltepe, J. S., Drakos, N. E., et al. 2023, The Astrophysical Journal, 954, 31, aDS Bibcode: 2023ApJ...954...31C
 Cheng, T.-Y., Conselice, C. J., Aragón-Salamanca, A., et al. 2020, MNRAS, 493, 4209
 Ćiprijanović, A., Snyder, G. F., Nord, B., & Peek, J. E. G. 2020, Astronomy and Computing, 32, 100390
 Croton, D. J. 2006, MNRAS, 369, 1808
 Davé, R., Anglés-Alcázar, D., Narayanan, D., et al. 2019, MNRAS, 486, 2827
 Dehghani, M., Djolonga, J., Mustafa, B., et al. 2023, Scaling Vision Transformers to 22 Billion Parameters
 Dewsnap, C., Barmby, P., Gallagher, S. C., et al. 2023, ApJ, 944, 137
 Dieleman, S., Willett, K. W., & Dambre, J. 2015, MNRAS, 450, 1441
 Domínguez Sánchez, H., Huertas-Company, M., Bernardi, M., Tuccillo, D., & Fischer, J. L. 2018, MNRAS, 476, 3661
 Dosovitskiy, A., Beyer, L., Kolesnikov, A., et al. 2021, An Image is Worth 16x16 Words: Transformers for Image Recognition at Scale
 Du, P., Hu, C., Lu, K.-X., et al. 2014, ApJ, 782, 45
 Euclid Collaboration, Bisigello, L., Conselice, C. J., et al. 2023, MNRAS, 520, 3529
 Ferreira, L., Conselice, C. J., Duncan, K., et al. 2020, ApJ, 895, 115
 Foreman-Mackey, D., Hogg, D. W., Lang, D., & Goodman, J. 2013, PASP, 125, 306
 Fukushima, K. 1988, Neural Networks, 1, 119
 Gabor, J. M., Impey, C. D., Jahnke, K., et al. 2009, ApJ, 691, 705
 Gardner, J. P., Mather, J. C., Clampin, M., et al. 2006, Space Sci. Rev., 123, 485
 Graham, A. W. & Scott, N. 2013, ApJ, 764, 151
 Grogin, N. A., Kocevski, D. D., Faber, S. M., et al. 2011, ApJs, 197, 35
 Gültekin, K., Richstone, D. O., Gebhardt, K., et al. 2009, ApJ, 698, 198
 He, K., Zhang, X., Ren, S., & Sun, J. 2015, arXiv e-prints, arXiv:1512.03385
 Hinshaw, G., Larson, D., Komatsu, E., et al. 2013, The Astrophysical Journal Supplement Series, 208, 19, aDS Bibcode: 2013ApJS...208...19H
 Hirschmann, M., Khochfar, S., Burkert, A., et al. 2010, MNRAS, 407, 1016
 Hoyos, C., den Brok, M., Verdoes Kleijn, G., et al. 2011, MNRAS, 411, 2439
 Huertas-Company, M., Gravet, R., Cabrera-Vives, G., et al. 2015, ApJS, 221, 8
 Huertas-Company, M., & Lanusse, F. 2023, PASA, 40, e001
 Huertas-Company, M., Primack, J. R., Dekel, A., et al. 2018, ApJ, 858, 114
 Jahnke, K. & Macciò, A. V. 2011, ApJ, 734, 92
 Ji, Z., Giavalisco, M., Kirkpatrick, A., et al. 2022, ApJ, 925, 74
 Kennedy, J. & Eberhart, R. 1995, in Proceedings of ICNN’95 - International Conference on Neural Networks, Vol. 4, 1942–1948 vol.4
 Kim, M., Ho, L. C., Peng, C. Y., Barth, A. J., & Im, M. 2008, ApJS, 179, 283
 Koekemoer, A. M., Faber, S. M., Ferguson, H. C., et al. 2011, ApJS, 197, 36
 Kormendy, J. & Ho, L. C. 2013, ARA&A, 51, 511

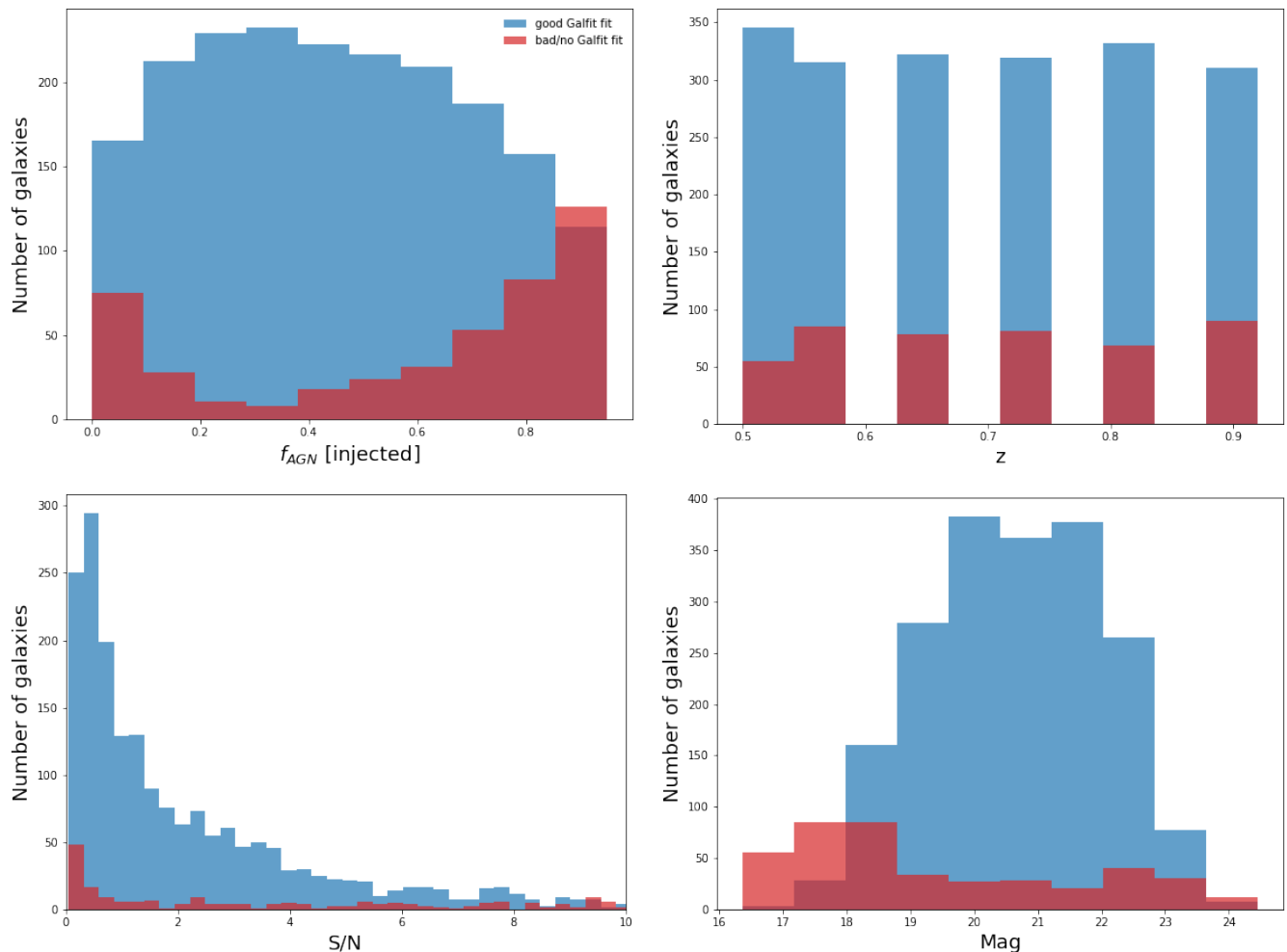


Fig. 11. Number of galaxies for which GALFIT returns a good fit (blue histograms) and for which there is a bad fit or no fit from GALFIT (red histograms), as a function of the injected AGN fraction (top left panel), redshift (top right panel), signal-to-noise ratio (bottom left panel) and magnitude (bottom right panel). While there is no obvious trend with redshift, GALFIT tends to fail for bright galaxies, galaxies with low S/N, or with very high or low injected AGN fractions.

Läsker, R., Ferrarese, L., van de Ven, G., & Shankar, F. 2014, ApJ, 780, 70
 LeCun, Y., Bengio, Y., & Hinton, G. 2015, Nature, 521, 436
 Li, J., Silverman, J. D., Ding, X., et al. 2021, ApJ, 918, 22
 Lintott, C. J., Schawinski, K., Slosar, A., et al. 2008, MNRAS, 389, 1179
 Liu, Z., Lin, Y., Cao, Y., et al. 2021, arXiv e-prints, arXiv:2103.14030
 Liu, Z., Mao, H., Wu, C.-Y., et al. 2022, Proceedings of the IEEE/CVF Conference on Computer Vision and Pattern Recognition (CVPR)
 Margalef-Bentabol, B., Huertas-Company, M., Charnock, T., et al. 2020, MNRAS, 496, 2346
 Margalef-Bentabol, B., Wang, L., La Marca, A., et al. 2024, A&A, 687, A24
 Marinacci, F., Vogelsberger, M., Pakmor, R., et al. 2018, MNRAS, 480, 5113
 Marshall, M. A., Wyithe, J. S. B., Windhorst, R. A., et al. 2021, MNRAS, 506, 1209
 Martin, G., Bazkiae, A. E., Spavone, M., et al. 2022, MNRAS, 513, 1459
 McConnell, N. J. & Ma, C.-P. 2013, ApJ, 764, 184
 Mechtley, M., Jahnke, K., Windhorst, R. A., et al. 2016, ApJ, 830, 156
 Mechtley, M. R. 2014, PhD thesis, Arizona State University
 Naiman, J. P., Pillepich, A., Springel, V., et al. 2018, MNRAS, 477, 1206
 Nelson, D., Pillepich, A., Springel, V., et al. 2018, MNRAS, 475, 624
 Nelson, D., Springel, V., Pillepich, A., et al. 2019, Computational Astrophysics and Cosmology, 6, 2
 Pearson, W. J., Suelves, L. E., Ho, S. C. C., et al. 2022, A&A, 661, A52
 Peng, C. Y. 2007, ApJ, 671, 1098
 Peng, C. Y., Ho, L. C., Impey, C. D., & Rix, H.-W. 2002, AJ, 124, 266
 Pierce, C. M., Lotz, J. M., Salim, S., et al. 2010, MNRAS, 408, 139
 Pillepich, A., Springel, V., Nelson, D., et al. 2018, MNRAS, 473, 4077
 Planck Collaboration, Ade, P. A. R., Aghanim, N., et al. 2016, A&A, 594, A13
 Rodriguez-Gomez, V., Genel, S., Vogelsberger, M., et al. 2015, MNRAS, 449, 49

Rodriguez-Gomez, V., Snyder, G. F., Lotz, J. M., et al. 2019, MNRAS, 483, 4140
 Schramm, M. & Silverman, J. D. 2013, ApJ, 767, 13
 Scoville, N., Aussel, H., Benson, A., et al. 2007, ApJS, 172, 150
 Simet, M., Chartab, N., Lu, Y., & Môbasher, B. 2021, ApJ, 908, 47
 Simmons, B. D., Lintott, C., Willett, K. W., et al. 2017, MNRAS, 464, 4420
 Somerville, R. S., Hopkins, P. F., Cox, T. J., Robertson, B. E., & Hernquist, L. 2008, MNRAS, 391, 481
 Son, S., Kim, M., Barth, A. J., & Ho, L. C. 2022, Journal of Korean Astronomical Society, 55, 37
 Springel, V., Pakmor, R., Pillepich, A., et al. 2018, MNRAS, 475, 676
 Sturm, M. R. & Reines, A. E. 2024, arXiv e-prints, arXiv:2406.06675
 Tuccillo, D., Huertas-Company, M., Decencière, E., et al. 2018, MNRAS, 475, 894
 Urbano-Mayorgas, J. J., Villar Martín, M., Buitrago, F., et al. 2019, MNRAS, 483, 1829
 Vaswani, A., Shazeer, N., Parmar, N., et al. 2017, arXiv e-prints, arXiv:1706.03762
 Walmsley, M., Allen, C., Aussel, B., et al. 2023, Journal of Open Source Software, 8, 5312
 Walmsley, M., Lintott, C., Géron, T., et al. 2022a, MNRAS, 509, 3966
 Walmsley, M., Scaife, A. M. M., Lintott, C., et al. 2022b, MNRAS, 513, 1581
 Walmsley, M., Smith, L., Lintott, C., et al. 2020, MNRAS, 491, 1554
 Weaver, J. R., Kauffmann, O. B., Ilbert, O., et al. 2022, The Astrophysical Journal Supplement Series, 258, 11, aDS Bibcode: 2022ApJS..258...11W
 Weinberger, R., Springel, V., Pakmor, R., et al. 2018, MNRAS, 479, 4056
 Willett, K. W., Galloway, M. A., Bamford, S. P., et al. 2017, MNRAS, 464, 4176
 Willett, K. W., Lintott, C. J., Bamford, S. P., et al. 2013, MNRAS, 435, 2835
 Zanisi, L., Huertas-Company, M., Lanusse, F., et al. 2021, MNRAS, 501, 4359
 Zhuang, M.-Y. & Ho, L. C. 2023, Nature Astronomy, 7, 1376
 Zhuang, M.-Y., Li, J., & Shen, Y. 2024, The Astrophysical Journal, 962, 93, aDS Bibcode: 2024ApJ...962...93Z

Appendix A: Results as a function of Sérsic index

We analyse how the performance of both methods depends on Sérsic index. In Fig. A.1 we compare the predicted f_{AGN} values from Zoobot and GALFIT for galaxies with low Sérsic index ($n < 1$) on the top panels and galaxies with high Sérsic index ($n > 6$) on the bottom panels. The results from Zoobot for low Sérsic index galaxies have RMSE = 0.035, $\langle \Delta f_{AGN} \rangle = 0.0027$ and $\sigma(\Delta f_{AGN}) = 0.035$, which corresponds to an increase of 30% in the RMSE. For high Sérsic galaxies, the performance is slightly better than the average for all galaxies, with RMSE = 0.020, $\langle \Delta f_{AGN} \rangle = 0.0004$ and $\sigma(\Delta f_{AGN}) = 0.021$. On the other hand, low Sérsic index galaxies have, from GALFIT results, a 47% worse RMSE compared to the whole test sample, with RMSE = 0.133, $\langle \Delta f_{AGN} \rangle = -0.048$ and $\sigma(\Delta f_{AGN}) = 0.12$, and it appears that the results are worse when not only the Sérsic index is low, but also the f_{AGN} (this is also seen in Fig. A.2), where we show how the RMSE varies in different bins of n for the whole sample, but also for galaxies with low and high AGN fraction ($f_{AGN} < 0.2$ and $f_{AGN} > 0.8$, respectively). A high Sérsic index does not seem to impact the predictions of f_{AGN} determined from GALFIT, with RMSE = 0.094, $\langle \Delta f_{AGN} \rangle = -0.005$ and $\sigma(\Delta f_{AGN}) = 0.094$.

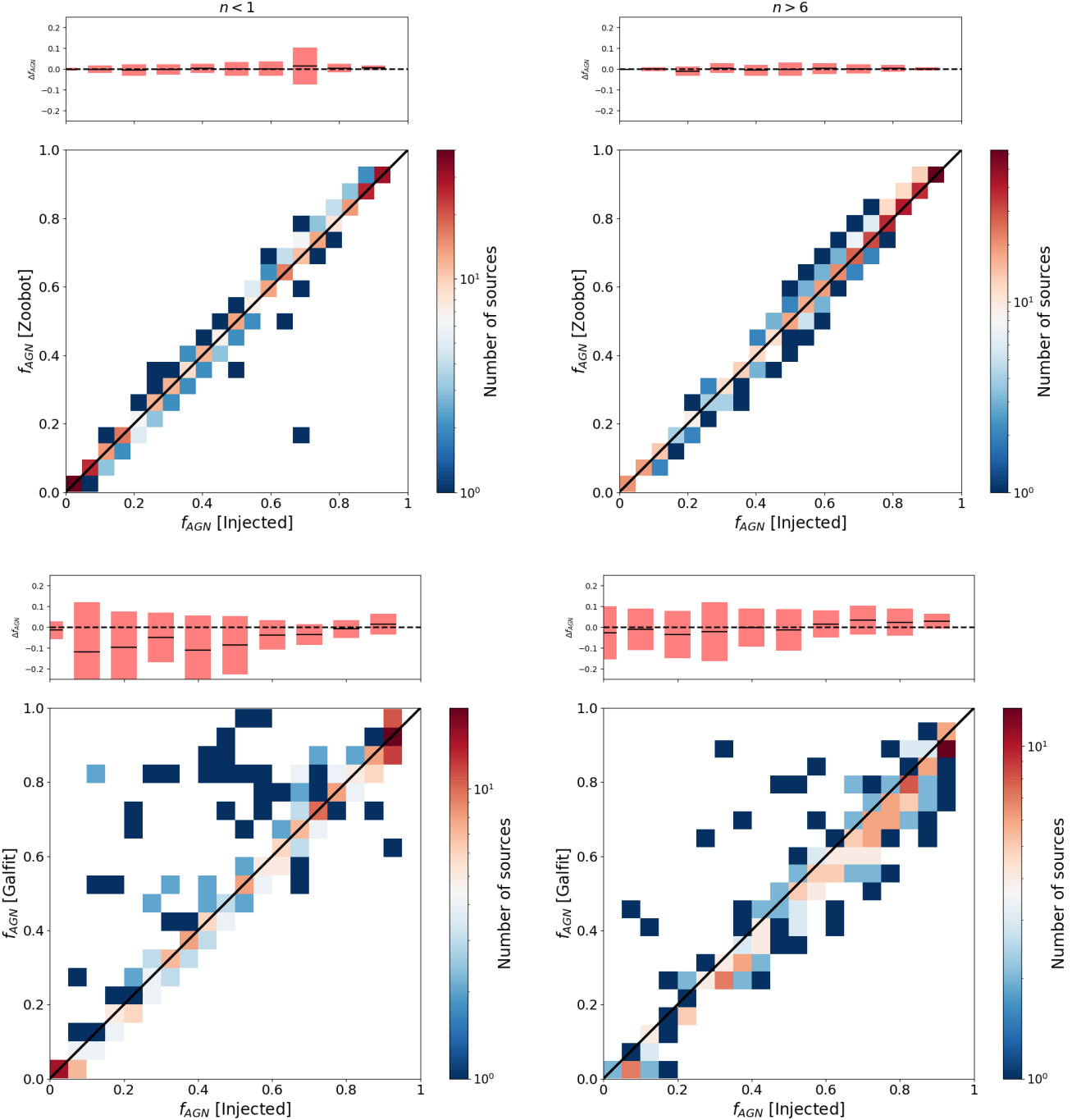


Fig. A.1. Comparison between the real injected AGN fraction and the recovered AGN fraction obtained from the Zoobot (top row) and GALFIT (bottom row), for galaxies with low Sérsic index ($n < 1$, left panels) and high Sérsic index ($n > 6$, right panels). The colour bar indicates the number of sources in each 2D bin.

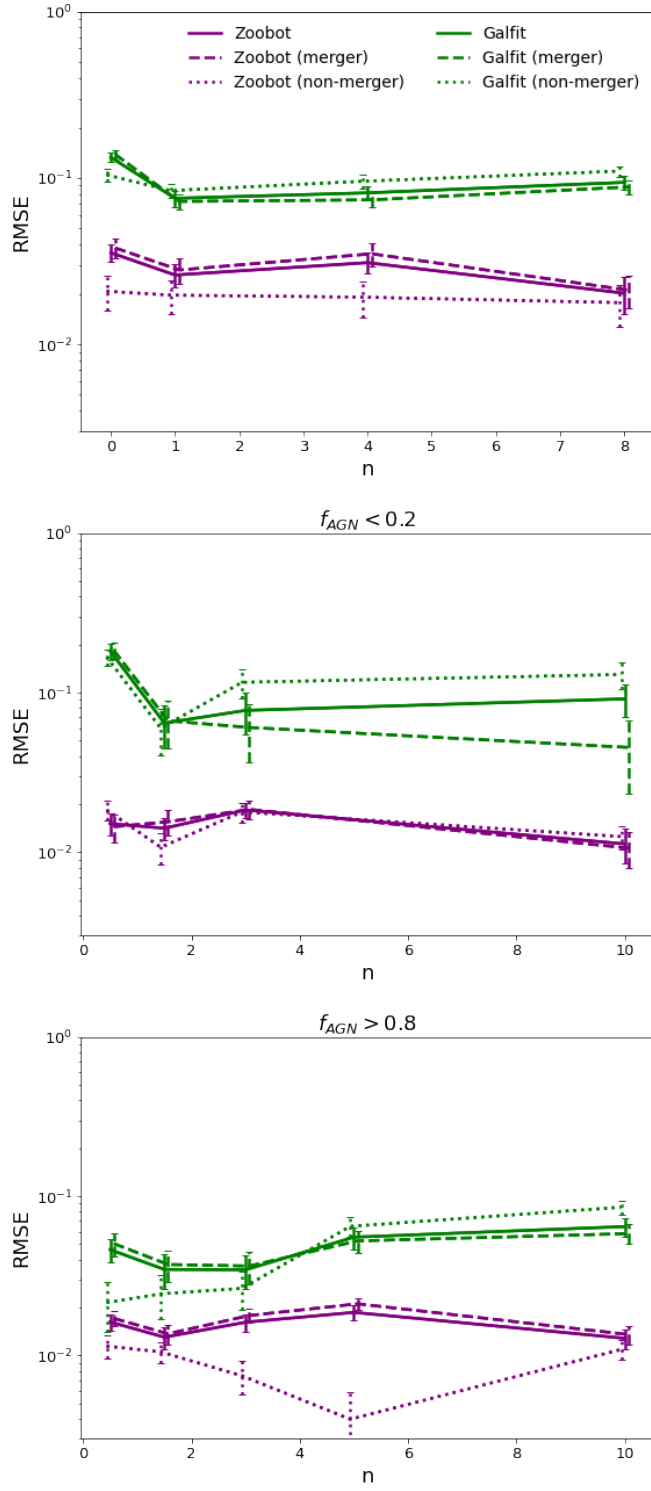


Fig. A.2. RMSE as a function of Sérsic index, for the whole sample (top panel), for galaxies with $f_{AGN} < 0.2$ (centre panel) and galaxies with $f_{AGN} > 0.8$ (bottom panel). The purple lines correspond to the results from Zoobot and the green lines from GALFIT. The solid lines correspond to the whole sample while the dashed and dotted lines correspond to the mergers and non-merger galaxies, respectively.